Circumnuclear regions in barred spiral galaxies II. Relations to host galaxies

J. H. Knapen[1,2], D. Pérez-Ramírez[3], S. Laine [4]

[1] *Isaac Newton Group of Telescopes, Apartado 321, E-38700 Santa Cruz de La Palma, Spain*
[2] *Department of Physical Sciences, University of Hertfordshire, Hatfield, Herts AL10 9AB, UK*
[3] *Department of Physics and Astronomy, Michigan Technological University, 1400 Townsend Dr., Houghton, MI 49931, USA*
[4] *Space Telescope Science Institute, 3700 San Martin Drive, Baltimore, MD 21218, USA*

arXiv:astro-ph/0207258v1 11 Jul 2002

ABSTRACT

We present optical broad- and narrow-band imaging of a sample of a dozen barred galaxies. These images are analyzed in conjunction with our previously published near-infrared imaging of their central regions and with literature values for, e.g., bar strengths and the total star formation activity of the galaxies. We present B, I and Hα images, and radial profiles derived from these, to infer geometric and dynamical parameters of the structural components of the galaxies, such as bar lengths, bar ellipticities, and location of star formation and dust. We find that the more centrally concentrated the Hα emission in a galaxy is, i.e., the higher the fraction of star formation originating in the circumnuclear region, the higher the overall star formation rate, as measured from far-infrared flux ratios. Stronger bars host smaller nuclear rings, but the strength of the bar does not correlate with either the intrinsic ellipticity of the ring or the offset between the position angles of the bar and the ring. We interpret these results in comparison with modelling of gas inflow in the circumnuclear region, and show that they were theoretically expected. We confirm observationally, and for the first time, the anti-correlation predicted from theory and modelling between the degree of curvature of the bar dust lanes and the strength of the bar, where stronger bars have straighter dust lanes.

Key words: galaxies: barred – galaxies: evolution – galaxies: ISM – galaxies: spiral – galaxies: starburst – galaxies: structure

1 INTRODUCTION

Most galaxies are barred (e.g., Sellwood & Wilkinson 1993; Knapen, Shlosman & Peletier 2000a) and a substantial fraction of barred galaxies show enhanced star formation (SF) activity in or near their centres, often in the form of complete or incomplete nuclear rings (e.g., Buta & Combes 1996; Knapen 1999). It is believed that there is a causal connection between the existence of a bar and circumnuclear SF activity. Through its non-axisymmetric potential, a bar can facilitate gas inflow by extracting angular momentum from the gas through gravitational torques. The inflowing gas may then accumulate in the vicinity of inner Lindblad resonances (ILRs), triggering massive SF (see, e.g., review by Shlosman 1999). It is therefore natural to infer that the properties of the circumnuclear starburst region are connected to those of the large-scale structure, most obviously the bar, and it is this inference that we wish to test observationally in the present paper.

Correlations have been established between morphological properties of the stellar bar, such as size, shape and surface brightness (Martin 1995; Elmegreen & Elmegreen 1985), the location of star forming regions (Sersic & Pastoriza 1967; Phillips 1993, 1996), the presence of nuclear activity (Chapelon, Contini & Davoust 1999; Knapen et al. 2000a; Shlosman, Peletier & Knapen 2000; Laine et al. 2002) and the Hubble type of their host galaxy. Bars are found to be longer in early-type barred galaxies (Martin 1995), longer bars are more elliptical (Martinet & Friedli 1997), bar radial profiles appear to be flatter in early-type galaxies and exponential in late-type galaxies (Elmegreen & Elmegreen 1985), and there is some evidence that the more elliptical the bar is, the higher is its overall SF rate (Aguerri 1999). There also appears to be some correlation between the location of SF in galaxies and their morphological classification. Phillips (1993) noted that early-type barred galaxies exhibit SF in rings but neither in the bar nor the centre, whereas

late-type barred spirals display many star forming regions along their bars.

Sersic & Pastoriza (1967) realised that enhanced SF is found in the inner parts of some spiral galaxies, and that this SF is frequently arranged into a ring or pseudo-ring pattern. Combes & Gerin (1985) and Athanassoula (1992a) found that such spiral galaxies are usually of early type and host a bar. Rings in galaxies, including nuclear rings, were extensively reviewed by Buta & Combes (1996). Buta & Crocker (1993) compiled a catalog of rings in galaxies, including ten nuclear rings studied in the present paper, and derived metric characteristics for the rings. Case studies combining optical and near-infrared (NIR) imaging with velocity fields and dynamical modelling show in detail how the bar and the circumnuclear regions (CNRs) are part of the same dynamical system. Gas is driven inward under the influence of a large stellar bar, where it piles up near or between the ILRs, and possibly results in massive SF. Examples of such case studies are those by Knapen et al. (1995a,b, 2000b) on M100 (=NGC 4321), Regan et al. (1996, 1997) on NGC 1530, Buta, Crocker & Byrd (1999) on ESO 565-11 (see also Rautiainen & Salo 2000), and Laine et al. (1999, 2001) and Jogee et al. (2002a,b) on NGC 5248. In thin bars (high axial ratio) the gas inflow may be most effective, but according to the simulations by Piner, Stone & Teuben (1995), nuclear rings will not form in such bars and gas will flow directly to the nucleus. Nuclear bars, spirals, or rings, are frequently observed on scales of a kiloparsec or less, and can be modelled as directly resulting from the dynamics of the overall system (see Knapen et al. 2001 for many examples).

We have performed an imaging study of a dozen barred spirals with evidence for the presence of star-forming CNRs, to investigate the coupling between the CNRs and their host galaxies in a more statistical manner. Our main goal is to test the hypothesis (Knapen et al. 1995b; Pérez-Ramírez & Knapen 1998) that the structure and dynamics of the large-scale bar and disk of the host galaxies is intimately connected with that of the inner, active region (either AGN or SF), and thus determines whether such activity occurs in a given galaxy, and in what form. In Paper I (Pérez-Ramírez et al. 2000), we presented NIR images of the central regions of a sample of 12 barred galaxies to study the properties of circumnuclear structures in stars and dust that exist at small scales (a few hundred pc to a few kpc). In this paper, we present optical broad-band and Hα imaging of the whole extent of the disks of the same 12 barred galaxies, and combine parameters derived from the NIR and optical parts of our imaging survey with parameters taken from the literature to identify several correlations which illuminate the important connections that exist between the central regions and the host galaxy structures at large.

We summarise the observations and data reduction procedures in § 2, and present our observational results in § 3. Relative Hα fluxes from different parts of the sample galaxies are explored in § 4. In subsequent sections, we explore correlations between the strength of the bar and the geometric parameters of the nuclear rings (§ 5), and the shapes of the dust lanes within the bar (§ 6). We summarise our main findings in § 7. Notes on individual objects can be found in Appendix 1.

Galaxy	Date	Telescope	Filters	Source
NGC 1300	11/98	JKT	B,I,Hα	This paper
NGC 1530	11/98	JKT	B,Hα	This paper
	10/96		I	JKT archive
NGC 2903	03/98	JKT	B,I,Hα	This paper
	11/98		B,I,Hα	This paper
NGC 3351	11/98	JKT	B,Hα	This paper
	04/99		I	JKT archive
NGC 3504	11/98	JKT	B,Hα	This paper
	04/98		I	JKT archive
NGC 3516	03/98	JKT	B,I,Hα	This paper
NGC 3982	11/98	JKT	B,Hα	This paper
	05/88		I	JKT archive
NGC 4303	11/98	JKT	B,Hα	This paper
	04/96		I	JKT archive
NGC 4314	03/98	JKT	B,Hα	This paper
	11/98		I	JKT archive
NGC 4321	05/92	INT	B,I	KB96
	04/91	WHT	Hα	K98
NGC 5248	04/95	INT	B,I,Hα	This paper
NGC 6951	10/95	INT	B,I	INT archive
	02/92	WHT	Hα	RBK96

Table 1. Observing details: month of observation (col. 2); telescope (col. 3), INT is the 2.5m Isaac Newton Telescope, WHT is the 4.2m William Herschel Telescope; filters (col. 4); and source from which the image was obtained (col. 5), KB96 is Knapen & Beckman (1996), RBK96 is Rozas, Beckman & Knapen (1996) and K98 is Knapen (1998)

2   OBSERVATIONS AND DATA REDUCTION

2.1   Optical observations

We present new and archival broad (B and I) and narrow-band (Hα) images of the entire bar and disk region of the 12 barred galaxies that make up our sample. The selection criteria and basic properties of our sample galaxies (spiral galaxies known to host star-forming circumnuclear ring-like structure) are given in Paper I. The main goal of the present paper is to identify and quantify basic structural parameters such as the bar length and ellipticity, the location and shape of dust lanes, and the distribution of massive SF. It is relatively easy to measure these parameters from multi-band optical imaging (see, e.g., Knapen et al. 1995a,b; Knapen & Beckman 1996). Schematically, we use different bands and colours as follows:

• I: to trace the old stellar population in the absence of significant contamination by young stars and dust. For most galaxies, we also used I-band images as the continuum that is subtracted from the raw Hα images,

• B: in combination with I, using $B − I$ colour index maps, to show the location of dust lanes and sites of SF,

• Hα: hydrogen recombination line emission to trace directly the massive SF.

Most images were obtained during two observing runs on the 1.0-m Jacobus Kapteyn Telescope (JKT), in 1998 March 2-9 and in 1998 November 9-15 (Table 1). We used the TEK4 CCD Camera with a pixel size of 0.331 arcsec/pixel, and a field of view (FOV) on the sky of 5.6×5.6 arcmin. The average FWHM seeing is just below 2 arcsec (best seeing is

1.2 arcsec). The images in I from the first run presented problems during the flat-fielding process. We have instead used I-band data for these galaxies from the Isaac Newton Group (ING) archive. In addition, we include several images from the literature, as detailed in Table 1.

2.2 Data reduction and photometric calibration

The images were reduced using standard IRAF tasks. First, the bias level of the CCD was subtracted from all exposures as a constant after we verified that the bias level was constant across the chip. The images were flat-fielded using sky flats taken in each filter at twilight. We estimated the sky background by determining the mean level on a few small areas in regions free of galactic emission, although later in the reduction we checked, and in some cases corrected, these estimates using the colour profiles (see § 2.3). The images were sky-subtracted and bias-only overscan regions were removed.

After foreground stars were located and their positions determined, we shifted all the images of each galaxy to a common position. Where multiple exposures in one band were available, these were median combined to make the final image of the galaxy in that band. Cosmic-ray events were automatically removed in the process. Again using the foreground stars, we calibrated the images astrometrically. The angle of rotation employed to achieve this was 181.2 degrees counterclockwise for the images from our two JKT runs.

The photometric calibration of the broad-band images of the galaxies was done using published aperture photometry where this was available. For the rest of the galaxies, we used a mean photometric constant. We could not use standard stars due to unfavourable weather conditions during both of our JKT runs. Our Hα data have not been calibrated for the same reason.

2.3 Ellipse fitting

After calibrating the images, we used the task ELLIPSE in IRAF to fit ellipses to the images, in order to produce radial runs of surface brightness in the different bands, as well as of parameters such as the major axis position angle (PA) and the ellipticity of the fitted ellipses. Unlike in Paper I, where foreground stars were not a problem because of the small FOV of the NIR images, here we had to select and mask out stars that could affect the fitting process. We first fitted one of the bands (I) leaving PA, ellipticity and centre position as free parameters in the fit. We then imposed the resulting radial runs of PA, ellipticity and centre position as fixed input values for the fits to the other two bands. That way, we ensure that when combining two bands to evaluate a colour (B-I in this case), we combine emission from the same areas in the individual images. $B - I$ radial profiles have the advantage that they are rather sensitive to uncorrect background subtraction in one of the individual images, which leads to easily recognizable sharply rising or dropping colour profiles in the outer regions. This fact allowed us to finetune the background subtraction, giving more accurate background determinations. We thus produced radial B, I and Hα surface brightness, $B-I$, PA and ellipticity profiles, all of which are shown in Fig. 1.

There was a problem in the practical implementation of this procedure for a few galaxies, for which the centre is saturated in our I-band image (NGC 4321, NGC 5248 and NGC 6951). We circumvented this problem by creating a fictitious centre. We located the real position of the centre from other bands, and added a number of counts to the pixel at this position (usually no more than 10% of the surrounding value) using the IRAF task PIXEDIT.

2.4 Colour index and Hα images

$B - I$ colour maps, which indicate the location of the major dust lanes in the disk of a galaxy, were produced by dividing one image by the other. Sky background levels were subtracted before doing this (see above). Correcting for different seeing values from one band to the other did not prove necessary. We also produced Hα line images, which are direct tracers of massive SF, by subtracting the continuum using the I-band images. We did not use narrow band continuum filters, since the use of I as a continuum filter gives sufficiently reliable results for our mostly morphological purposes, with a considerable saving in observing time. To determine the scaling factor to be used for the continuum subtraction in our new images we followed a procedure based upon the one described by Böker et al. (1999). We first found the pixel by pixel intensity correlation in the original I and Hα images, using CORMAP (a GIPSY task). Most pixels in our large images trace background or galaxy continuum, emission from which which will, after appropriate scaling, be equal in the two filters. This factor will mostly depend on the shape of the throughput curves of the filters used. All these pixels will fall along a straight line, the x and y intercepts of which give an additional estimate for the sky background in the I and Hα images. The minority of pixels which trace Hα line emission will have enhanced Hα emission relative to I (continuum), and will be displaced toward higher Hα values in the diagram. Most pixels thus fall on the easily identifiable straight line indicating the continuum scaling factor for this particular set of two images (Hα line and continuum), and this factor is determined simply by measuring the slope of the correlation line. Once we determined the scaling factor, we subtracted the scaled galactic continuum.

We considered the final subtraction successful when no bumps or hollows were observed when checking the central region of the final image. More extensive testing of this method, including a comparison with a method where fluxes from foreground stars are used to derive the continuum scaling factor, and a comparison of different filters (R, I, narrow-band continuum filter centred at $\lambda = 6470$Å and 115Å wide) used for continuum subtraction, will be presented elsewhere (Knapen et al., in preparation). From that study, and from tests performed in this paper, we conclude that scaling factors can be determined accurately as described above, and that resulting uncertainties in the Hα flux level are of the order of 1% in the disk to at most 10% in the H II regions closest to the nucleus. The bulk of the latter uncertainty originates in colour differences between the wavelength of the on- and off-line filters, in turn mostly caused by excess dust extinction in the CNR at the Hα wavelength as compared to that of the I filter. The continuum subtraction for the Hα images of NGC 4321 and NGC 6951 was done differ-

ently, and has been described by Knapen (1998) and Rozas et al. (1996), respectively.

2.5   NIR observations

We obtained broad-band NIR images of the central few kpc regions of our sample galaxies, as described in detail in Paper I. The sub-arcsecond resolution NIR images were obtained with the Canada-France-Hawaii Telescope. In Paper I, we present the data in the form of sets of greyscale and contour plots of the broad-band images and of colour index images derived from them, and sets of radial profiles of surface brightness, colour, ellipticity and PA. In Fig. 2, we show overlays of the central regions of the Hα images, described in § 2.1 and § 2.4, on the NIR $J - K$ colour index images from Paper I.

3   OBSERVATIONAL RESULTS

3.1   Morphology of the disks and CNRs

In Fig. 1, we show for each galaxy greyscale representations of the I broad-band, $B - I$ colour index, and Hα narrow-band images, radial profiles of PA and ellipticity as determined from the fit to the I-band image, and radial surface brightness (B, I and Hα) and colour ($B - I$) profiles. In the top left corner of each panel of the figure we show the Hα continuum-subtracted emission from the CNR, on the same scale as the NIR images in Paper I. Many circumnuclear features, often in the shape of more or less complete rings (e.g., NGC 1300, NGC 3351, NGC 4314, NGC 6951) or spiral arm-like features (e.g., NGC 1530, NGC 4321) can easily be distinguished. Except in NGC 3516 and NGC 4314, Hα emission from the spiral arms in the disk is obvious. Some of the bars (e.g., those in NGC 1530, NGC 3504, NGC 5248) show clear signs of massive SF, whereas others (e.g., those in NGC 1300, NGC 3351, NGC 4303, NGC 6951) are completely devoid of Hα emission. The $B - I$ colour index maps show (in lighter tones, indicating bluer colours) predominantly where SF occurs at present, mostly in the CNR and the disk spiral arms, but also (in darker tones, indicating redder colours) where the main dust lanes are located. While organised dust lanes are often seen outlining spiral arms in the disk, we will in the present paper concentrate on the dust lanes in the bars, which are thought to outline the locations of shocked gas, and are thus prime tracers of the bar dynamics (see § 6).

In Fig. 2, we present overlays of the Hα emission (in contours) from the CNR on the $J - K$ colour index images from Paper I for all sample galaxies. In general, the location of the nuclear ring in Hα corresponds to that in the NIR, but in several cases the Hα is more extended (e.g., NGC 1300, NGC 3516, NGC 3982, NGC 4303). More specific details on individual galaxies are summarised in Appendix 1.

3.2   Bar and CNR parameters

We summarise selected properties of the sample galaxies in Tables 2 and 3, as taken from the literature and from Paper I, and as derived in this paper. Table 2 lists the scale in parsec/arcsec, the morphological type, type of nuclear activity, and a brief description of the observed CNR features for all sample galaxies. We determined the scale length of the exponential disk of each galaxy by least-squares fitting of the relevant part of the I-band surface brightness profile (Fig. 1). The dimensions of the nuclear ring were measured directly from the images, and are given in Table 3 as major and minor axis sizes, in kpc. The size of the ring was measured by tracing the ridge line of the ring from the colour index maps (for the NIR) or the Hα images (for the SF), and fitting these coordinates to an ellipse to find the size and the ellipticity. Allowing for the different kinds of imaging used, our ring dimension measurements generally agree rather well with those published by Buta & Crocker (1993) for the ten galaxies common to their and our samples. We also derived the relative size and deprojected (or intrinsic) ellipticity of the nuclear rings, which are listed in Table 3. Typical uncertainties in these quantities are 10% and 0.05, respectively. The relative size of the ring was defined as the diameter of the ring divided by the diameter of the disk, where we use D_{25} from the RC3 to find the latter value. Laine et al. (2002) showed that the distribution of these relative nuclear ring sizes peaks at $r_{\rm ring}/D_{25} = 0.06$. The values found here are in agreement with their result.

We used the NIR and optical radial profiles in combination with the images to measure the difference between the PAs of the nuclear ring and of the bar. Using the disk parameters given in Table 2 we deprojected this angle. The final PA offset between the bar and the ring is given in Table 3. Typical uncertainties, resulting from small uncertainties in the PAs as measured from the profiles and images and in the deprojection parameters, are $\pm 7°$.

The basic bar parameters length and ellipticity are also tabulated in Table 3. We define the end of the bar as the radius where the ellipticity reaches its local maximum value. The uncertainty in the bar length is on the order of 5% – 10%. The bulge component usually has a radius of only 1 kpc or so, and is not expected to affect the measured bar lengths. We used the scales as given in Table 2 to calculate the values in kpc, and the disk parameters (Table 2) to deproject the bar ellipticities and lengths.

To evaluate the ellipticities of the bars, often, but strictly speaking incorrectly, referred to as bar strengths, we followed the simple procedure outlined by Martin (1995), and implemented by many other authors (e.g., Martinet & Friedli 1997; Chapelon et al. 1999; Knapen et al. 2000a). Considering bars to be ellipsoidal features, their shape can be described by the ellipticity of the bar $\epsilon = 1 - b/a$ (where b/a is the bar axis ratio). A value of $\epsilon = 0$ corresponds to the absence of a bar, whereas $\epsilon = 0.8$ denotes the thinnest class of bars. Following the approach of, among others, Knapen et al. (2000a), we have determined the bar ellipticity from the maximum in the radial ellipticity profile in a region of roughly constant PA. This value is then deprojected using the (disk) ellipticity at large radii in the disk of the galaxy, and the difference between the bar PA and the PA of the major axis of the outer disk. The results are listed in Table 3, where typical uncertainties in the ellipticity measures are 0.05.

Recently, bar strength has been addressed in a more accurate sense on the basis of NIR imaging, basically by measuring the ratio of non-axisymmetric to axisymmetric forces

Galaxy	Scale pc/arcsec	Morphological type	Nuclear activity	CNR feature	Disk scale length (kpc)	Disk PA (°)	Inclination angle (°)
NGC 1300	101	(R')SB(s)bc	–	Ring	21.5	87	35
NGC 1530	159	SB(rs)b	–	Ring+spiral	9.6	8	45
NGC 2903	36	SAB(rs)bc	Starburst	Ring	3.4	22	65
NGC 3351	49	SB(r)b	Starburst	Ring	1.9	13	40
NGC 3504	99	(R)SAB(s)ab	Starburst	Ring+spiral	2.0	147	22
NGC 3516	171	(R)SB(s)	Sy 1.5	Ring	4.2	46	34
NGC 3982	72	SAB(r)b	Sy 2	Spiral	0.6	6	14
NGC 4303	101	SAB(rs)a	Sy 2	Ring	5.7	116	22
NGC 4314	62	SB(rs)a	LINER	Ring+spiral	3.2	59	27
NGC 4321	70	SAB(s)bc	–	Ring+spiral	3.1	153	30
NGC 5248	74	SAB(rs)bc	–	Ring+spiral	3.3	105	40
NGC 6951	92	SAB(rs)bc	LINER/Sy	Ring+spiral	3.7	157	44

Table 2. Properties of the sample galaxies. NGC number (col. 1), scale (col. 2, Paper I); morphological type (col. 3, from de Vaucouleurs et al. 1991, hereafter RC3), presence and type of nuclear activity (col. 4, from NED; Sy is Seyfert), features in the CNR (col. 5, Paper I), scale length of the exponential disk (col. 6), and deprojection parameters: PA of the major axis of the outer disk (col. 7) and galaxy inclination (col. 8).

| Galaxy	Dimensions of Hα ring (kpc)	Ring size	Ring ϵ Deproj.	PA offset (°) Deproj.	Bar Length (kpc)	Bar ellipticity ϵ	ϵ_d	Bar strength Q_b	$\Delta\alpha$ (°/kpc)
NGC 1300	0.5×0.5	0.026	0.18	28	8.6	0.72	0.58	0.44	5
NGC 1530	0.7×0.6	0.032	0.19	85	11.0	0.61	0.65	0.71	3
NGC 2903	0.4×0.2	0.030	0.17	18	2.7	0.60	0.15	0.26	-
NGC 3351	0.7×0.6	0.064	0.11	88	3.1	0.39	0.58	0.20	12
NGC 3504	0.4×0.3	0.050	0.10	43	2.9	0.62	0.36	0.26	11
NGC 3516	——	–	–	–	2.4	0.30	0.39	-	-
NGC 3982	——	–	–	–	0.8	0.41	0.37	-	-
NGC 4303	0.6×0.6	0.030	0.07	53	4.3	0.54	0.58	0.27	9
NGC 4314	0.5×0.4	0.064	0.27	12	4.8	0.63	0.67	0.33	7
NGC 4321	0.9×0.6	0.058	0.26	19	3.7	0.50	0.50	0.20	18
NGC 5248	0.9×0.9	0.066	0.23	10	7.8	0.48	0.51	0.03	20
NGC 6951	0.5×0.3	0.046	0.29	46	5.5	0.50	0.52	0.39	0

Table 3. Properties of the nuclear rings and the bars in our sample galaxies: measured dimensions of the nuclear ring (major and minor axis radii, in kpc, col. 2), ring size expressed as $D_{\rm ring}/D_{25}$, where D_{25} is from the RC3 (Col. 3), deprojected ring ellipticity (col. 4), deprojected (col. 5) PA offset (in degrees) between major axes of the nuclear ring and of the bar; deprojected bar length in kpc (col. 6); bar ellipticity as determined from our data, as measured (col. 7) and deprojected (col. 8); bar strength $Q_{\rm b}$ (col. 9; from Block et al. 2001, E. Laurikainen & H. Salo, in preparation, and R. Buta, private communication; the average is given where a galaxy is included in more than one study); and dust lane curvature measure $\Delta\alpha$ (see text, col. 10).

(e.g., Buta & Block 2001; Block et al. 2001; Laurikainen, Salo & Rautiainen 2002). Determinations of the bar strength parameter $Q_{\rm b}$ by Block et al. and Laurikainen et al. in general agree well (E. Laurikainen, private communication), but only broad agreement between this bar strength and the bar ellipticity has been found (Block et al. 2001). In Table 3, we also list values for $Q_{\rm b}$ for those galaxies where this has been determined. Typical errors in $Q_{\rm b}$ are ±0.1.

With the information in hand, we can easily check the correlation between the bar "strength" and length, as reported by Martinet & Friedli (1997). In Fig. 3a, we show how the length of the bar is correlated with the strength of the bar, as measured through $Q_{\rm b}$. This figure at first sight indeed confirms the claim by Martinet & Friedli that stronger bars are longer. But if instead of the bar length in kpc the length of the bar relative to the scale length of the exponential disk of its host galaxy is plotted (Fig. 3b), the correlation disappears, and there is even a hint that shorter bars are stronger, which is opposite to the effect reported by
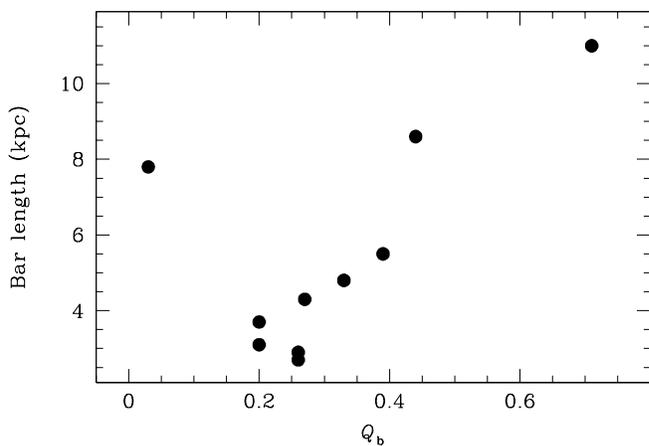
Figure 3. a. Bar length in kpc as function of bar strength. Typical uncertainties are 5-10% in bar length and 0.1 in $Q_{\rm b}$.
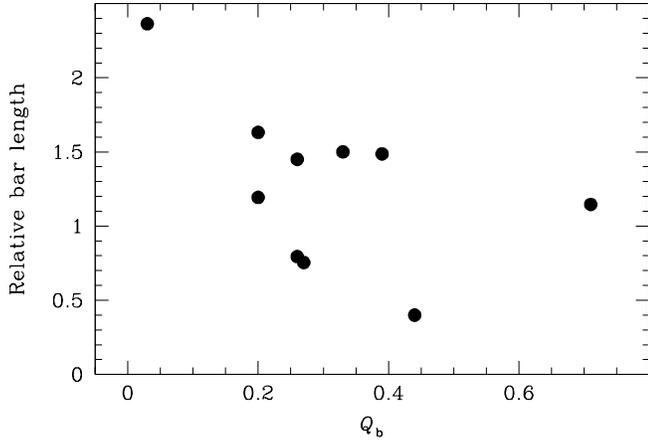
Figure 3. b. Relative bar length, or the ratio of bar length and disk exponential scale length, as function of bar strength. Typical uncertainties are 10-15% in relative bar length and 0.1 in Q_b.
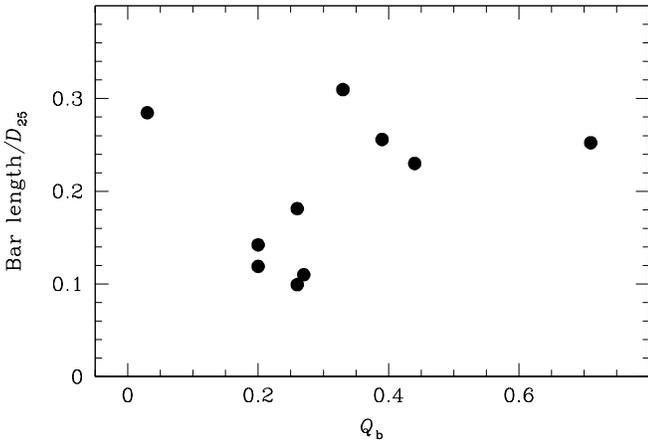
Figure 3. c. As Fig. 2b, but now for the ratio of bar length and galaxy size. The RC3 parameter D_{25} was used for the latter value.

Martinet & Friedli (1997). Reproducing the measure used by Martinet & Friedli, bar length relative to the size of the host galaxy (D_{25} from the RC3), we find no correlation at all (Fig. 3c). Reasons for the confusing set of results may include the small sample size in our study, but also the use by Martinet & Friedli of parameters measured by Martin (1995), who derived bar lengths and ellipticities from optical (as opposed to NIR) images, and who used bar ellipticity as a measure of bar strength. Proper analysis of a larger galaxy sample is needed to confirm any relation between lengths and strengths of galactic bars. We draw attention to a deviant point in Fig. 3a,b, which denotes the very weak bar in NGC 5248 ($Q_b = 0.03$). This may well be a special case, as described in detail by Jogee et al. (2002a,b).

3.3 Radial profiles

Some of the most important morphological characteristics of each galaxy can be recognised in radial profiles such as the ones shown in Fig. 1. In NGC 4321, Knapen & Beckman (1996) identified four main regions in the Hα profile,

reflected also in, e.g., the $B - I$ profile: the nuclear area corresponding to a central peak and explained by the existence of enhanced SF in and around the nucleus; the bar region with a relatively smaller SF rate, seen as a dip in the profile; a region where the Hα luminosity falls off exponentially, which corresponds to the star forming spiral arms in the disk; and finally an outer region of steeper decline. From their study of H II region distributions in spiral galaxies, González Delgado & Pérez (1997) note that the barred galaxies in their sample tend to have either rising or flat central parts in the radial distribution of the number of H II regions per unit surface area, which is probably connected to the lack of SF in the bar. It is interesting in this respect that the one exception mentioned by González Delgado & Pérez (1997) is NGC 7479, well-known for being a strongly barred galaxy with exceptionally prominent SF within the bar, a bar which may have been created in a recent minor merger (Laine & Heller 1999).

We can now try to generalise findings such as those by Knapen & Beckman (1996) using the 12 Hα radial profiles for the barred galaxies in our sample. Considering primarily the Hα profiles, we find that most galaxies have enhanced emission in the CNR, although in some cases non-stellar emission from the nucleus may contribute to a central rise in the profile (e.g., in NGC 3516). Very often the profile shows a dip in the region of the bar. Particularly good examples are NGC 1300, NGC 3351 and NGC 6951. In a number of galaxies, such as in NGC 1530, the profile shows a small rise corresponding to zones of enhanced SF near the ends of the bar, clearly visible in the images. The inner rings near the ends of the bar in NGC 3351 and NGC 3504 can be recognised as bumps in the Hα profile. A few galaxies (e.g., NGC 4303 and NGC 6951) clearly show the SF in the disk outside the bar region, just as in NGC 4321 (Knapen & Beckman 1996). In the case of NGC 2903 there is a dominant continuous component in the profile, and individual star forming regions are hard to identify. We can conclude that the radial zones identified by Knapen & Beckman (1996) in their study of NGC 4321 are not all present in each of the galaxies studied here. However, depending on the distribution of SF in the galaxies, morphologically important regions can be recognised in the profiles, such as the CNR with enhanced, or the bar with depressed SF. In general, and as expected, the results obtained from the radial profiles are consistent with the morphology as summarised in Appendix 1.

Where specific zones are seen in the Hα profile, these can usually be recognised in the B and I profiles as well. These profiles behave in a very similar way radially: central peak; depression in the bar region, less pronounced in I, as expected for an older, redder, bar population; inner ring where present; and exponential disk. The $B - I$ colour index profile also follows the large-scale distribution of SF in most galaxies, showing a blue peak in the CNR and a red depression in the bar zone.

4 RELATIVE Hα FLUX FROM BARS AND CIRCUMNUCLEAR REGIONS

In order to study whether and how the large-scale parameters of disks of galaxies influence the relative distribution of the massive SF within those disks, we have measured

Galaxy	% Flux from the disk (excluding bar and CNR)	% Flux from the bar (excluding CNR)%	% Flux from the CNR (excluding nucleus)
NGC 1300	67	24	9
NGC 1530	31	37	29
NGC 2903	68	19	13
NGC 3351	51	10	38
NGC 3504	6	20	66
NGC 3516	11	0	45
NGC 3982	91	0	0
NGC 4303	69	19	12
NGC 4314	0	17	74
NGC 4321	73	11	16
NGC 5248	63	14	20
NGC 6951	77	7	15

Table 4. Relative flux from the disk, bar and circumnuclear regions. The latter does not contain the flux from the nuclear point source, if present, which is also why the percentages given here do not add up to 100% in all galaxies. Typical uncertainties are 25%, 10% and a few to 10% for disk, bar and CNR values, respectively (see text).

the relative Hα flux from the bars and the CNRs. We have done this by separating the images into different regions: the CNR, the bar and the disk, and determining the flux from these areas with the aperture photometry package within GAIA. The separation of the Hα images into individual areas was done by carefully judging where the CNR and bar regions end, which is in general very easy to recognise in Hα (see Fig. 1), but also referring to the I and $B - I$ images in doing so. While this may well introduce a small uncertainty in our measurements, the main source of uncertainty, especially for the entire disk, is the determination of the background sky value. The resulting uncertainties are of the order of 25% in the flux from the total disk, 10% in the case of the bar, and one to a few % in the CNRs. Given the uncertainties in the continuum subtraction in the nuclear regions (see §2.4), we conservatively increase the error margin for the CNR flux ratio to 10%.

For NGC 3516 and NGC 3982 no bar could be defined, and no bar flux values for these galaxies are included in the table. In order to take out possible disturbing effects due to Hα emission from active nuclei, we subtracted the flux from a nuclear point source, where present, from the CNR flux. Only in one galaxy (NGC 3516) is the nuclear Hα flux fraction high (44%) and hard to determine, and we do not consider this galaxy in the analysis below. Of the three galaxies with nuclear flux fractions of 8%-9%, in two the nuclear point source is easy to identify (NGC 3982 and NGC 4314, see Fig. 1g,i), whereas in NGC 3504 the uncertainty is slightly higher. In all other galaxies, the nuclear Hα flux fraction is zero or low (0-3%) and relatively easy to determine. Table 4 lists the relative fluxes thus obtained for the CNR, bar, and disk, for our sample galaxies.

In certain sample galaxies (NGC 3504 and NGC 4314) the Hα flux from the CNR dominates the total Hα emission from the host galaxy. The relative contribution of the bar itself is substantial in galaxies such as NGC 1300 and NGC 1530, but is generally at the level of around 10% of the total flux. The contribution from the disk is very small or even negligible in NGC 3504, NGC 3516 and NGC 4314, substantial or dominant in all others.
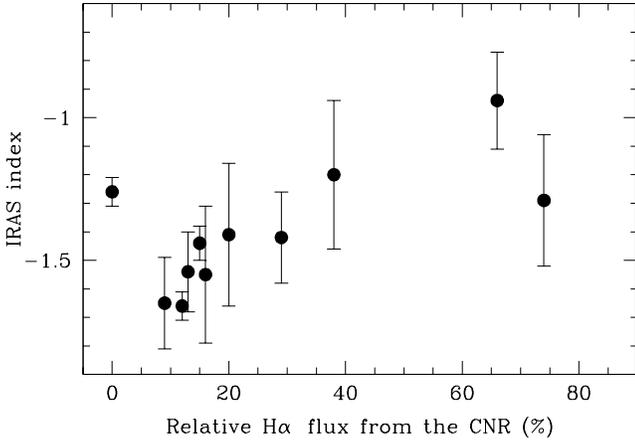
Various authors have used far-infrared (FIR) colour indices as direct estimators of current SF activity. Pux-
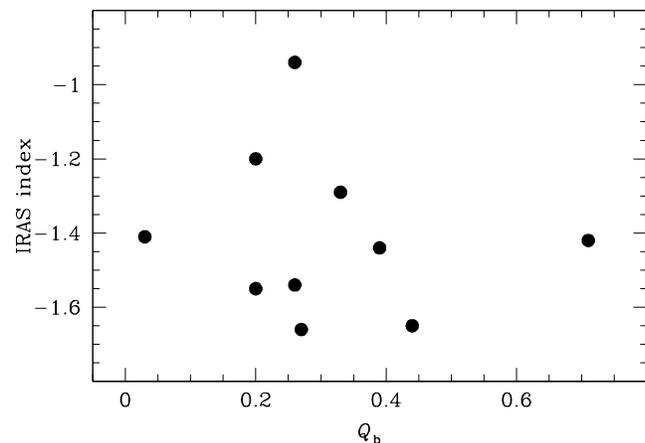
Figure 4. IRAS index $\log(S_{25}/S_{100})$ as a function of the strength of the bar, Q_b.
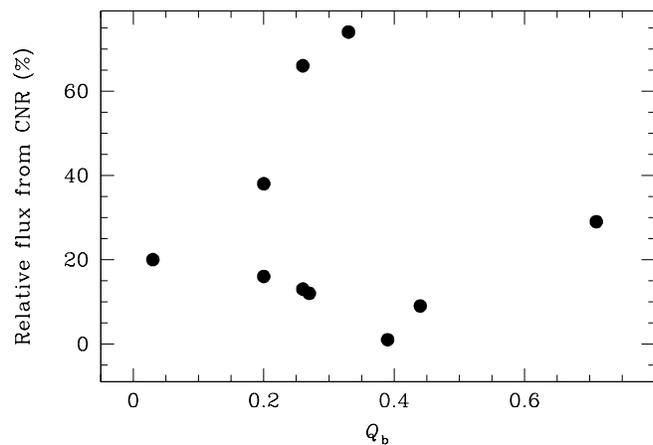
Figure 5. Relative flux from the CNR (excluding the nucleus), plotted as a function of the strength of the bar, Q_b.

Figure 6. Relative flux from the CNR (excluding the nucleus) vs. the IRAS index $\log(S_{25}/S_{100})$. Typical errors along the x-axis are a few to ten percent (see text).

Figure 7. Difference between the major axis PAs of the nuclear ring and the bar which hosts it, as a function of bar strength Q_b. Typical uncertainties are 7% in PA offset and 0.1 in Q_b.

ley, Hawarden & Mountain (1988) established a value of $\log(S_{12}/S_{25}) < -0.35$ as a signature of the existence of regions of SF. Dultzin-Hacyan, Moles & Masegosa (1988) studied a sample of H II galaxies and discussed the use of $\log(S_{25}/S_{100})$ to evaluate the SF activity, giving median values of $\log(S_{25}/S_{100}) = -1.4$ for normal galaxies, -1.15 for LINERs, -0.8 for starburst and Seyfert 2 galaxies, and -0.5 for Seyfert 1 galaxies. Martinet & Friedli (1997), using the same parameter, considered two classes of FIR colours ($\log(S_{25}/S_{100}) \geq -1.2$ and $\log(S_{25}/S_{100}) < -1.2$) corresponding to more or less pronounced SF activity, respectively.

We have compiled IRAS fluxes for our sample galaxies from the literature (Table 5). We explored possible relations between the IRAS index $\log(S_{25}/S_{100})$, used as an indicative value to quantify the global SF, and the length and strength of the bars, but found no trends from our small sample of galaxies (e.g., Fig. 4 shows the IRAS index vs. bar strength Q_b). From larger samples of galaxies, but using less reliable methodology, Martinet & Friedli (1997) and Aguerri (1999) found that galaxies with enhanced global SF as measured from their IRAS fluxes tend to have longer and more elliptical bars[*]. Equally, we cannot distinguish any trends in the distribution of SF as a function of bar strength Q_b (as an example, we show the run of the relative flux from the CNR against bar strength in Fig. 5) or length (not shown) of the bar. A related conclusion is drawn by Sheth (2001) who finds that the ratio of nuclear over disk molecular gas surface density does *not* correlate with the length of the bar. This ratio itself is much enhanced in barred with respect to non-barred galaxies (see also Sakamoto et al. 1999) .

Figure 6 presents the run of the relative flux from the CNR against the IRAS $\log(S_{25}/S_{100})$ index, quantifying the global SF. It shows that a higher Hα flux fraction from the CNR leads to higher IRAS indices. This may be due to the IRAS index being more sensitive to CNR SF, which is concentrated in a more dusty environment than disk SF. It may also imply, though, that the more centrally concentrated the

[*] Note that both these studies used bar parameters determined from optical imaging, and that Aguerri did not de-project these parameters.
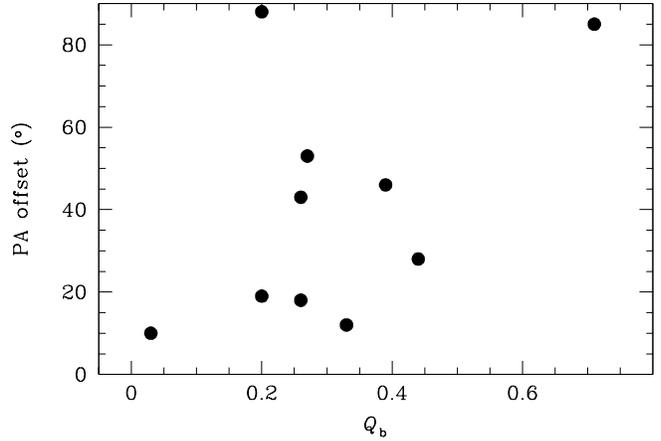
star formation is, the more SF takes place in absolute terms in the whole of the host galaxy. Although we subtracted the Hα flux which might be a result of non-stellar nuclear activity rather than circumnuclear SF, a caveat here is the role played by nuclear activity in the FIR emission, which we cannot quantify for our sample galaxies in the absence of FIR spectroscopy. On the basis of studies of other galaxies (see e.g. Genzel & Cesarsky 2000), though, we estimate that the Seyfert nucleus contributes at most 20%, and possibly as little as 5%, to the total flux, with the exception of NGC 3516. For this galaxy, already excluded from our analysis on other grounds, Mouri & Tanaguchi (2002) claim that the FIR luminosity is dominated by the AGN contribution. Only the study of a larger sample of galaxies can confirm the tentative relation we report here. We have started to undertake such a larger study.

5   ORIENTATION OF BARS AND NUCLEAR RINGS

From our Hα images and radial profiles we have measured the sizes of the nuclear rings, the deprojected differences between the PAs of the major axes of the rings and of the large-scale bar of their host galaxies, as well as the deprojected, or intrinsic, ellipticities of the rings (Table 3). Since for most of our galaxies we also know the bar strength, we can now, for the first time, explore observationally how these geometric ring parameters depend on the strength of the bar potential that hosts them.

The relative orientations of the nuclear rings span the complete range from aligned to perpendicular to the bar, with no preferred PA offset. This was also found by Buta & Crocker (1993). These authors describe a number of caveats in the derivation of PA offsets which also apply to our work, namely selection effects, sample size, and difficulty of properly defining ring shapes and orientation. In Fig. 7, we plot the observed PA offset between the nuclear ring and the bar as a function of the bar strength Q_b. Even though the galaxy with the weakest bar (NGC 5248) has the smallest PA offset

Galaxy	S_{25} (W m^{-2} Hz^{-1})	% error	S_{100} (W m^{-2} Hz^{-1})	% error	$\log(S_{25}/S_{100})$
NGC 1300	2.30E−27	0	1.03E−25	10	−1.65±0.16
NGC 1530	8.40E−27	7	2.19E−25	9	−1.42±0.16
NGC 2903	2.90E−26	6	1.01E−24	7	−1.54±0.14
NGC 3351	2.09E−26	12	3.35E−25	18	−1.20±0.26
NGC 3504	3.73E−26	9	3.27E−25	16	−0.94±0.17
NGC 3516	8.94E−27	7	2.26E−26	6	−0.40±0.04
NGC 3982	8.33E−27	3	1.52E−25	3	−1.26±0.05
NGC 4303	1.40E−26	1	6.47E−25	3	−1.66±0.05
NGC 4314	3.62E−27	12	7.14E−26	13	−1.29±0.23
NGC 4321	1.57E−26	11	5.62E−25	11	−1.55±0.24
NGC 5248	1.74E−26	12	4.45E−25	13	−1.41±0.25
NGC 6951	1.37E−26	3	3.75E−25	3	−1.44±0.06

Table 5. IRAS flux values for our sample galaxies, as obtained from Moshir et al. (1990)
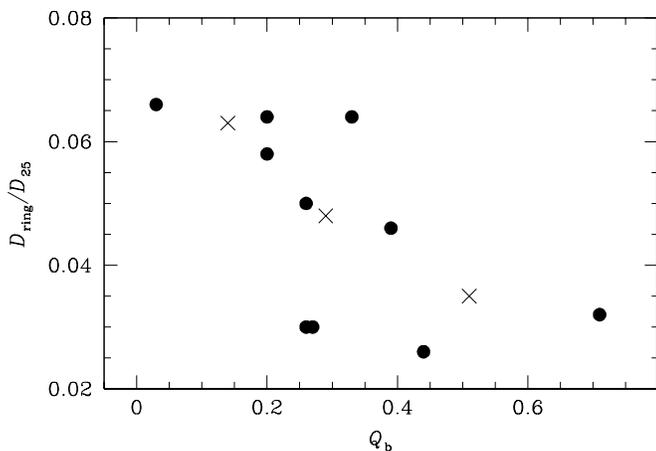
Figure 8. Relative size of the nuclear ring (ring diameter divided by D_{25} of the galaxy) as a function of bar strength Q_b (filled dots). Typical uncertainties are 10% in relative ring size and 0.1 in Q_b. Crosses indicate averages of the data points with Q_b values between 0 and 0.25 (3 galaxies), 0.26 and 0.35 (4), and 0.39 and 1 (3), respectively.
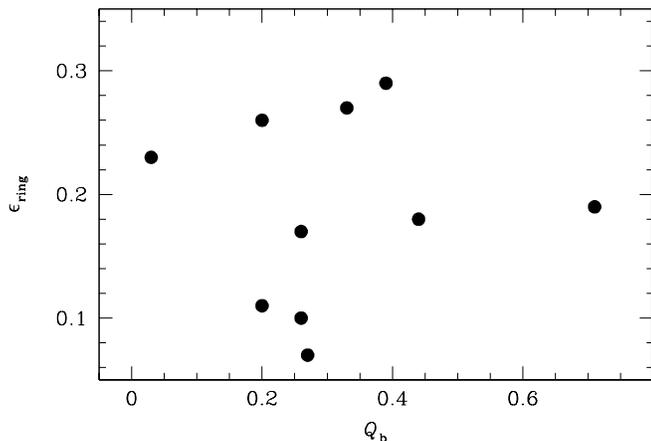

Figure 9. Deprojected, or intrinsic, ellipticity of the nuclear ring as a function of bar strength Q_b. Typical uncertainties are 0.05 in ring ϵ and 0.1 in Q_b.

and the one with the strongest bar (NGC 1530) one of the largest, there is no obvious correlation.

Fig. 8 shows the run of the relative size of the nuclear ring, defined as the ring diameter divided by the host galaxy diameter, as a function of bar strength Q_b. It is seen that stronger bars host smaller rings. Finally, Fig. 9 shows that the intrinsic ellipticity of the rings does not vary with different bar strength.

Numerical modelling (e.g., Knapen et al. 1995b; Heller & Shlosman 1996) gives important clues to the evolution of the geometric properties of a nuclear ring which forms near the ILRs in a barred galaxy. The first point to note is that stronger, thinner, bars lead to smaller nuclear rings, exactly as we see here in Fig. 8. This can be seen, e.g., in fig. 11 of Knapen et al. (1995b), from the form and extent of the representative stellar periodic orbits in a bar with ILRs. The main orbit family, that of the so-called $x1$ orbits (see Contopoulos & Papayannopoulos 1980), forms the backbone of the stellar bar. A second orbit family, that of the $x2$ orbits, is oriented perpendicularly to the $x1$ orbits in the region of the ILRs. Since nuclear rings are gaseous features, it is important to note that gas can only populate those regions where the $x1$ and $x2$ orbits are not intersecting, which is the inner part of the galaxy. Fig. 11 of Knapen et al. (1995b) makes clear that, in order to avoid the intersecting orbits, gas will have to settle further in in the case of stronger, or thinner, bars. This then leads to smaller areas where the nuclear ring can form, and thus to smaller nuclear rings. Of course smaller nuclear rings in this context is a relative term, and we have chosen here to use the size of the ring relative to the total size of the galaxy (following Laine et al. 2002). However, if we use the size of the ring relative to the length of the bar as a measure, we find a similar correlation (not shown) as depicted in Fig. 8.

The situation is different for both the PA offsets from the bar, and the intrinsic ellipticities, of the nuclear rings. As described by, e.g., Knapen et al. (1995b) and Shlosman (1999), these parameters are regulated primarily by the gas inflow into the CNR. As can be seen in, e.g., fig. 13 of Knapen et al. (1995b), less inflow will lead to a smaller leading angle of the ring with respect to the bar, and to a smaller ellipticity of the ring: it becomes rounder. Since gas inflow does not depend exclusively on the parameters of the bar, such as its strength, but more generally on the availability
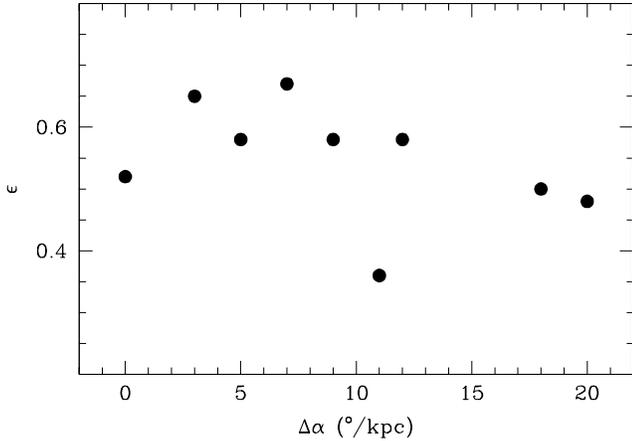
Figure 10. Deprojected ellipticity of the bar as a function of dust lane curvature index $\Delta\alpha$. Straight dust lanes in the bar are on the left side of the diagram, and thin bars are towards the top. Typical uncertainties are 0.05 in bar ϵ and $3°$/kpc in $\Delta\alpha$.

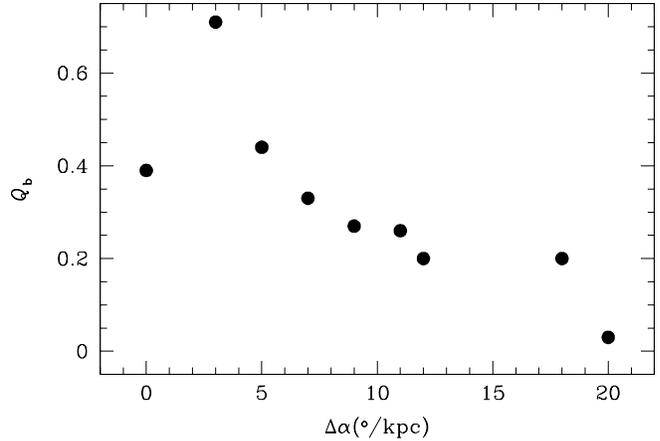**Figure 11.** As Fig. 10, but now with bar strength Q_b. Typical uncertainty in Q_b is 0.1.

of fuel, correlations of ring ellipticity and PA offset are not expected, and in fact not observed (Figs. 7, 9). The dynamical timescale in the CNR is of the order of 10^7 yrs, and thus the availability of the fuel can be expected to be variable, further eliminating any correlation with, e.g., the bar strength. Because the dynamical timescale of a large stellar bar is much longer ($\sim 10^8$ yrs) the size of a nuclear ring will be much more stable in time, given the arguments outlined in the preceding paragraph. This picture is nicely illustrated by the recent results of Jogee et al. (2002b) for the nuclear ring of NGC 5248. They found that the younger population in the ring, as traced by FUV emission, outlines spiral arms and is more elliptical in shape, whereas the relaxed ring, as seen in older stellar population, is much rounder.

6   BARS AND DUST LANES WITHIN THEM

Colour index maps reveal interesting symmetric dust lane patterns in the bars of strongly and weakly barred galaxies. The curvature of the dust lanes has theoretically been related to the strength of the bar, in the sense that weak bars are associated with curved dust lanes, whereas strong bars have straight dust lanes (Athanassoula 1992b).

We have used a simple method to measure and quantify the curvature of the dust lanes, in an attempt to probe the anti-correlation theoretically predicted by Athanassoula (1992b) between the degree of curvature of the bar dust lanes and the strength of the bar. From deprojected $B - I$ and B-band images, where the dust lanes are well visible, we have measured the change in the angle of the tangent to the curved dust lane, and express the result $\Delta\alpha$ in units of degrees per kiloparsec distance along the dust lane. We ignore those parts of the dust lanes (e.g., where the lanes connect to the CNR) where the curvature increases or decreases sharply. Well-defined, twofold symmetric dust lanes could not be identified clearly enough in NGC 2903, NGC 3516, and NGC 3982, and these galaxies are not considered in the analysis below.

In this scheme, the lowest values of $\Delta\alpha$ correspond to the straightest class of dust lanes (e.g., NGC 6951), whereas

the highest values obviously correspond to the most curved lanes (e.g., NGC 5248). The measurements were made along the largest possible stretch of dust lane, which in all cases runs from just outside the CNR to very near the end of the bar. Since dust lanes have rather constant curvature over this entire range, use of a smaller part of the lanes to derive $\Delta\alpha$ would lead to the same values, but with larger uncertainties simply because the linear range involved would be smaller. We estimate typical errors in $\Delta\alpha$ to be of the order of $3°$/kpc, where uncertainties in the distance to the galaxy, and in the definition of the curvature of the dust lane from the images are the main contributing factors. The resulting values are tabulated in Table 5 and plotted against deprojected bar ellipticity in Fig. 10, and against Q_b in Fig. 11.

The theoretically expected trend of more curvature of the dust lanes in weaker bars is borne out clearly in the run of Q_b vs. dust lane curvature, but much less clearly so, if at all, in the run of bar ellipticity. This is in fact the first time that a correlation between bar strength and dust lane curvature has been *observed* for a sample (albeit admittedly small) of bars. We thus confirm observationally the prediction from theory and modelling (e.g., Athanassoula 1992b). The fact that the correlation shows up much less clearly when bar ellipticity is considered does not contradict this confirmation, given the poor correlation between bar ellipticity and Q_b shown by Block et al. (2001). We looked for, but did not find, correlations between the curvature of the dust lanes and parameters like host galaxy type or inclination angle.

7   SUMMARY

This paper is the second of a pair presenting results of our study of how the general structure of barred galaxies is related to, and possibly determines, the presence and properties of dynamical features such as rings and spirals in their CNRs. We present optical broad and narrow-band imaging of our sample galaxies in B, I and Hα in order to map the structural components across the disks of these barred galaxies. The 12 galaxies in our sample are all nearby spiral galaxies known to host star-forming circumnuclear ring-like structure. We present graphically our optical images and the

radial profiles we derived from these by ellipse fitting. From these data, we infer geometric and dynamical parameters such as bar lengths and ellipticities, and location of SF and general dust structures, and combine these with parameters obtained from the literature.

Our main results can be summarised as follows:

• For the first time using bar strengths (Q_b values from the literature) rather than ellipticity, and using NIR imaging of the bars, we checked the previously found correlation between bar strength and length, i.e., longer bars are also stronger. Our results are confusing because bar length as such correlates with bar strength, but bar length relative to, e.g., the size of the galaxy does not. Careful study of larger samples is needed.

• The FIR index $\log(S_{25}/S_{100})$, a SF indicator, is used to verify whether the strength of the bar is connected to the global SF activity. We find no relation with the bar strength Q_b nor with the length of the bar.

• We measure the relative Hα flux from the disk, bar and CNR components in the galaxies. We find that the more centrally concentrated the Hα emission is (i.e., the higher the fraction of total SF from the CNR), the more SF takes place in absolute terms in the galaxy, as estimated from the FIR flux ratios. This is possibly due to the IRAS index being more sensitive to CNR SF, which is concentrated in a dust-rich environment. Alternatively, the CNR SF activity as measured from Hα is related to the overall SF activity, as measured in the FIR, of the disk. We find no correlation between the relative Hα flux from the disk, the bar, and the CNR with bar strength, nor with bar length.

• We explore relations between the strength of the bar and the geometric parameters of the nuclear rings, namely their size relative to the galaxy disk, intrinsic inclination, and PA offset between the major axes of the nuclear ring and the bar which hosts it. We find that stronger bars tend to host smaller rings, but that the bar strength is unrelated to both the PA offset and the intrinsic ring ellipticity. The fact that smaller rings occur in stronger bars can be understood from bar orbit theory, which predicts that stronger bars limit the region where $x2$ orbits can exist, and thus in turn the size of the nuclear ring. As known from numerical modelling, both PA offset and intrinsic ring ellipticity depend primarily on the mass inflow rate into the nuclear ring, which in turn is determined only in part by the strength of the bar, but more directly on the availability of fuel, and on temporal variations therein.

• We present a new, reproducible, measure of the curvature of dust lanes in bars, a parameter which was theoretically linked about a decade ago to the strength of the bar. This link is through gas shocking under the influence of the bar potential, at the location where pairs of symmetric dust lanes are seen along the bars in optical images. We indeed confirm that the stronger the bar, the straighter its dust lanes. This is in fact the first observational confirmation of this theoretical result, based on the use of both a sample (admittedly still rather small) of galaxies, and of quantitative measures of both dust lane curvature and bar strength.

From these results, we can confirm that indeed the CNRs of barred galaxies are intimately linked to their host galaxies, and that their SF and morphological properties are determined to a significant degree by the properties of,

mainly, the large bar. The small size of our sample precludes a detailed exploration of the correlations that we have found. Studies using larger samples of nuclear ring galaxies are needed to more fully test the predictions and results from theory and modelling, and to explore further relations between the parameters governing the CNR, the bar, and the disk.

REFERENCES

Aguerri J. A. L., 1999, A&A 351, 43
Alonso-Herrero A., Ryder S. D., Knapen J. H., 2001, MNRAS, 322, 757
Athanassoula E., 1992a, MNRAS, 259, 328
Athanassoula E., 1992b, MNRAS, 259, 345
Benedict G. F., et al., 1993, AJ, 105, 1369
Block D. L., Puerari I., Knapen J. H., Elmegreen B. G., Buta R., Stedman S., Elmegreen D. M., 2001, A&A, 375, 761
Böker T. et al. 1999, ApJS, 124, 95
Buta R., Block D. L., 2001, ApJ, 550, 243
Buta R., Combes F., 1996, Fundamentals of Cosmic Physics, 17, 95
Buta, R. & Crocker, D. A. 1993, AJ, 105, 1344
Buta, R., Crocker, D. A., & Byrd, G. G. 1999, AJ, 118, 2071
Chapelon S., Contini T., Davoust, E., 1999, A&A, 345, 81
Colina L., Arribas S., 1999, ApJ, 514, 637
Colina L., García Vargas M. L., Mas-Hesse J. M., Alberdi A., Krabbe A., 1997, ApJ, 484, L41
Combes F., Gerin M., 1985, A&A, 150, 327
Contopoulos G., Papayannopoulos T., 1980, A&A, 92, 33
de Vaucouleurs G., de Vaucouleurs A., Corwin J. R., Buta R. J., Paturel G., Fouque P., 1991, Third reference catalogue of Bright galaxies, 1991, New York : Springer-Verlag (RC3)
Downes D., Reynaud D., Solomon P. M., Radford S. J. E. 1996, ApJ, 461, 186
Dultzin-Hacyan D., Moles M., Masegosa J., 1988, A&A, 206, 95
Elmegreen B. G., Elmegreen, D. M., 1985, ApJ, 288, 438
Friedli D., Wozniak H., Rieke, M., Martinet L., Bratschi P., 1996, A&AS, 118, 461
Genzel R. & Cesarsky C. J. 2000, ARAA, 38, 761
González Delgado R. M. & Pérez E. 1997, ApJS, 108, 199
Jogee S., Knapen J. H., Laine S., Shlosman I., Scoville N. Z., 2002a, ApJ, 570, L55
Jogee S., Shlosman I., Laine S., Englmaier P., Knapen J. H., Scoville N. Z., Wilson C. D., 2002b, ApJ, in press (astro-ph/0202270)

Knapen J. H. 1998, MNRAS, 297, 255

Knapen J. H., 1999, in ASP Conf. Ser. 187, The Evolution of Galaxies on Cosmological Timescales, eds. J. E. Beckman, & T.J. Mahoney (San Francisco: Astronomical Society of the Pacific), 72

Knapen J. H., Beckman J. E., 1996, MNRAS, 283, 251

Knapen J. H., Beckman J. E., Shlosman I., Peletier R. F., Heller C. H. & de Jong R. S., 1995a, ApJL, 443, L73

Knapen J. H., Beckman J. E., Heller C. H., Shlosman I. & de Jong R. S., 1995b, ApJ, 454, 623

Knapen J. H., Beckman J. E., Shlosman I., & Mahoney T. J., Eds., 2001, ASP Conf. Ser. 249: The Central Kiloparsec of Starbursts and AGN: The La Palma Connection (San Francisco: Astronomical Society of the Pacific)

Knapen J. H., Shlosman I., Heller C. H., Rand R. J., Beckman J. E. & Rozas, M., 2000b, ApJ, 528, 219

Knapen J. H., Shlosman I., Peletier R. F., 2000a, ApJ, 529, 93

Laine S., & Heller C. H., 1999, MNRAS, 308, 557

Laine S., Knapen J. H., Pérez-Ramírez D., Doyon R., Nadeau D., 1999, MNRAS, 302, L33.

Laine S., Knapen J. H., Pérez-Ramírez D., Englmaier P., Matthias M., 2001, MNRAS, 324, 891

Laine, S., Shlosman, I., Knapen, J. H., Peletier, R.F., 2002, ApJ, 567, 97

Laurikainen E., Salo H., Rautiainen P., 2002, MNRAS, 331, 880

Martin P., 1995, AJ, 109, 2428

Martinet L., Friedli D. 1997, A&A, 323, 363

Moshir, M., et al., 1990, IRAS Faint Source Catalogue, version 2.0 (Pasadena: JPL Infrared Processing and Analysis Center)

Mouri, H. & Taniguchi, Y. 2002, ApJ, 565, 786

Pérez–Ramírez, D., Knapen J. H. 1998, in IAU Symp. 184, The Central Regions of the Galaxy and Galaxies, ed. Y. Sofue (Dordrecht: Kluwer), 113

Pérez–Ramírez D., Knapen J. H., Peletier R. F., Laine S., Doyon R., Nadeau D., 2000, MNRAS, 317, 234 (Paper I)

Phillips A. C. 1993, A&AS, 183, 2306

Phillips A. C., 1996, in ASP Conf. Ser. 91, Barred galaxies, eds. R. Buta, D. A. Crocker, B. G. Elmegreen (San Francisco: Astronomical Society of the Pacific), 44

Piner B. G., Stone J. M., & Teuben P. J. 1995, ApJ, 449, 508

Pogge R. W., 1989, ApJS, 71, 433

Puxley P. J., Hawarden T. G., Mountain C.M. 1988, MNRAS, 231, 465

Rautiainen P. & Salo H. 2000, A&A, 362, 465

Regan M. W., Teuben P.J., Vogel S.N., van der Hulst, T. 1996, AJ, 112, 2549

Regan M. W., Vogel S. N., Teuben P. J., 1997, ApJ, 482, L143

Rozas M., Beckman J. E., Knapen J. H. 1996, A&A, 307, 735

Sakamoto K., Okumura S. K., Ishizuki S., Scoville N. Z., 1999, ApJ 525, 691

Sellwood J. A. & Wilkinson A. 1993, Rep. Prog. Phys., 56, 173

Sersic J. L., Pastoriza M. G. 1967, PASP, 79, 152

Sheth K., 2001, in ASP Conf. Ser. 249, The Central Kiloparsec of Starbursts and AGN: The La Palma Connection, eds. J. H. Knapen, J. E. Beckman, I. Shlosman, & T. J. Mahoney (San Francisco: Astronomical Society of the Pacific), 605

Shlosman I., 1999, in ASP Conf. Ser. 187, The Evolution of Galaxies on Cosmological Timescales, eds. J. E. Beckman, & T.J. Mahoney (San Francisco: Astronomical Society of the Pacific), 100

Shlosman I., Peletier R. F., Knapen J. H., 2000, ApJ, 535, L83

Wozniak H., Friedli D., Martinet L., Martin P., Bratschi P., 1995, A&AS, 111, 115

APPENDIX A: NOTES ON INDIVIDUAL GALAXIES

A1 NGC 1300

This barred galaxy is a prototype grand-design SBb spiral. It has a very prominent and smooth bar and two spiral arms that start abruptly at the end of the bar (Fig. 1a). In our $B - I$ image, we can see two straight, offset dust lanes rather parallel to the major axis of the bar. These dust lanes are smooth when compared to the arms, which corresponds to a lack of distinct emitting regions. It is also apparent from our colour map that, near the ends of the bar, the bar dust lanes join the dust lanes along the inner edge of the arms. SF is not obvious in the bar, nor in the nucleus. The CNR is a site of considerable SF, concentrated in a small area. There is a concentration of HII regions where the arms join the bar, and mainly so on the western side. The western arm also contains several very luminous HII regions, while the eastern arm shows some less luminous enhancements. The Hα profile shows a modest peak of luminosity at radii corresponding to those of the CNR, and a gradual decrease in the region of the bar. The radial profiles reflect and confirm the distribution of SF in this galaxy.

The nuclear ring in NGC 1300 (Fig. 1a, 2a) is rather small angularly, and our Hα image does not give much information. It is clear, however, that the massive SF occurs in a number of discrete clumps (see also Pogge 1989), which are not reproduced in the NIR colour index images. Whereas the nuclear ring is incomplete in Hα, it appears complete in the NIR, although in Paper I we showed that the NIR ring is in fact a pair of tightly wound spirals. The *HST* image (fig. 1 of Paper I) shows structure in the nuclear ring, but no hot spots corresponding to the Hα emission peaks.

A2 NGC 1530

NGC 1530 (Fig. 1b) has a large and moderately elliptical bar and two wide open spiral arms originating from its ends. Its most prominent feature, however, is a bright mini-spiral at a radius of $10''$ from the nucleus, and extended roughly perpendicularly to the bar. This feature can be seen best in the Hα and $B - I$ images. From CO and HI observations (e.g., Downes et al. 1996; Regan et al. 1996) it is known that a large amount of gas is present in the centre. Despite this, the galaxy has a relatively modest SF rate near the nucleus, which can be explained by the trapping of gas in x_2 orbits near an inner ILR, inhibiting further infall. The gas will thus not reach the critical density that is needed to make the galaxy a true starburst (Downes et al. 1996). In our Hα image, we find relatively weak SF sites along the bar, at the ends of the bar, and along the spiral arms. In the CNR we find two distinct strongly emitting regions, from where the arms of the mini-spiral seem to start. The Hα profile shows a peak at the centre, dips in the region of the bar, and a slight increase at roughly the radius where the bar joins the disk spiral arms. Our $B - I$ image shows two curved dust lanes emerging from the nucleus, which continue along the bar. Again, as in NGC 1300, it is apparent from our colour map that, near the ends of the bar, the bar dust lanes join those along the inner edge of the arms.

The two symmetrically placed clumps of massive SF (Fig. 1b, 2b) are not obvious in the colour map, and seem to be hidden by the spiral structure. They appear similar to K1 and K2 in M100 (Knapen et al. 1995a), however, whereas

Figure 1. Images and photometric profiles for the 12 galaxies in our sample. The lower left panel is a contour plus greyscale plot of the galaxy in the I-band. Contour levels are indicated in the captions to the individual galaxy figures. The coordinates are J2000.0, obtained from the NASA/IPAC Extragalactic Database (NED). The panels in the middle show a greyscale representation of the $B - I$ colour index (below) and Hα images. A close-up of the centre of the Hα image is presented on the upper left, showing exactly the same region as that shown for the NIR imaging in fig. 1 in Paper I, to facilitate intercomparison. Darker tones indicate redder colours in the $B - I$ image, more flux in Hα. The right panels show radial profiles of, from bottom to top, B, I and Hα surface brightness, $B - I$ colour, PA and ellipticity. The B and I-band surface brightness and $B - I$ colour have been photometrically calibrated using aperture photometry from the literature, while the Hα surface brightness is uncalibrated and given in instrumental units of log(counts). All profiles are plotted as a function of major axis radius. The PA has been measured in degrees from N through E. Small filled dots in the PA and ellipticity profiles are the NIR values reproduced from fig. 1 of Paper I. Uncertainties due to the fitting procedure have not been indicated in the figure because they are smaller than the symbol size in all cases, except for the colour index profile at large radii, where uncertainties can amount to $0.1 - 0.3$ mag for the outer few points plotted. **a.** NGC 1300. Contours from I=21 to 20 mag arcsec^{-2}, with intervals of 0.25 mag arcsec^{-2}, and from 19.5 to 17 with intervals of 0.5; greyscale levels in I from 21.5 to 17 in steps of 0.25.

Figure 1. b. NGC 1530. Contours and grey levels from I=21.5 to 17 mag arcsec^{-2} in steps of 0.5 mag arcsec^{-2}.

Figure 1. c. NGC 2903. NIR PA and ellipticity were not fitted in Paper I and have not been plotted. Contours and grey levels from I=20.0 to 16.25 mag arcsec^{-2} in steps of 0.25 mag arcsec^{-2}.

Figure 1. d. NGC 3351. Contours and grey levels from I=20.5 to 16 mag arcsec^{-2} in steps of 0.25 mag arcsec^{-2}. Differences between the PSFs of the B and I images cause some small artifacts in the $B - I$ image.

Figure 1. e. NGC 3504. Contours and grey levels from I=21.5 to 15.5 mag arcsec^{-2} in steps of 0.5 mag arcsec^{-2}.

Figure 1. f. NGC 3516. Contours and grey levels from I=21.5 to 15.5 mag arcsec^{-2} in steps of 0.5 mag arcsec^{-2}.

Figure 1. g. NGC 3982. Values for $\mu_{B,I}$ and $B - I$ are averages as determined from the other sample galaxies, the data for this galaxy have themselves not been calibrated. Contours from I=17.2 to 16.4 mag arcsec^{-2} in steps of 0.2 mag arcsec^{-2}, grey levels starting at I=19.0 mag arcsec^{-2} but otherwise the same.

Figure 1. h. NGC 4303. Contours and grey levels from I=20.75 to 16.0 mag arcsec^{-2} in steps of 0.25 mag arcsec^{-2}.

Figure 1. i. NGC 4314. Values for μ_I and $B - I$ are averages as determined from the other sample galaxies, the data for this galaxy have themselves not been calibrated. Contours and grey levels from I=20.0 to 15.5 mag arcsec^{-2} in steps of 0.25 mag arcsec^{-2}.

Figure 1. j. NGC 4321. The nuclear region in the I-band image is saturated, and no data are available in that region in the I and $B - I$ images and the I and $B - I$ profiles. Contours and grey levels from I=22.0 to 17.5 mag arcsec^{-2} in steps of 0.5 mag arcsec^{-2}.

Figure 1. k. NGC 5248. The nuclear region in the I-band image is saturated, and no data are available in that region in the I and $B - I$ images and the I and $B - I$ profiles. Contours and grey levels from I=21.0 to 16.5 mag arcsec^{-2} in steps of 0.5 mag arcsec^{-2}

Figure 1. l. NGC 6951. The nuclear region in the I-band image is saturated, and no data are available in that region in the I and $B - I$ images and the I and $B - I$ profiles. Values for μ_I and $B - I$ are averages as determined from the other sample galaxies, the data for this galaxy have themselves not been calibrated. Contours and grey levels from I=19.25 to 16.5 mag arcsec^{-2} in steps of 0.25 mag arcsec^{-2}.

Figure 2. a. Hα contours over a greyscale $J - K$ colour map of NGC 1300. Contour levels are linearly increasing in instrumental counts. Darker tones in the colour index image indicate redder colours. **b.** As Fig. 2a, now for NGC 1530.

Figure 2. c. As Fig. 2a now for NGC 2903. **d.** Hα contours (as in Fig. 2a) overlaid on a greyscale representation K-band image of NGC 3351.

Figure 2. e. As Fig. 2a now for NGC 3504. **f.** As Fig. 2a, now for NGC 3516.

Figure 2. g. As Fig. 2a now for NGC 3982. **h.** As Fig. 2a, now for NGC 4303.

in M100 K1 and K2 are most obvious in the NIR, the peaks are not conspicuous at all in our NIR images of NGC 1530, not even in the *HST* image (Paper I). Hα emission is seen to follow the northern miniature spiral arm, coinciding with the red spiral arm fragment in the NIR colour index image.

A3   NGC 2903

NGC 2903 is a "hot-spot" galaxy with a circumnuclear starburst. The $B - I$ colour map reveals a beautiful and complex multi-armed dust structure, but no clear pair of dust lanes in the bar (Fig. 1c). In the Hα images we see SF along the bar and in the arms, mostly in the southern arm, and in the CNR. Very luminous HII regions delineate the bar and arms in this galaxy. The Hα profile drops smoothly, outlining continuous and strong HII emission all the way from the centre to the ends of the bar, and further out into the disk. The profiles show a lot of structure throughout the CNR and disk, caused by the combined effects of dust extinction and SF activity. Blue dips in the $B - I$ profile are accompanied by enhancements in the Hα and in some cases the B profiles. No NIR PA and ellipticity profiles are given because these could not be fitted in Paper I.

The Hα emitting regions do not all correspond in position and intensity to the NIR hot spots (Fig. 2c). Our Hα image shows just three of them, whereas our ground-based NIR images, and especially the *HST* NIR image (Paper I), show a plethora of individual emitting regions. A detailed study of the SF properties of the CNR in this galaxy, using *HST* archival Hα and Pa α imaging and NIR spectroscopy, in combination with stellar population synthesis modelling, has recently been published by Alonso-Herrero, Ryder & Knapen (2001).

A4   NGC 3351

NGC 3351 shows a nuclear ring and a larger, inner, ring of HII regions that encircles the stellar bar (Fig. 1d). The $B - I$ image shows two straight dust lanes emerging from an elliptical ring-like region surrounding the nuclear ring. The SF in this galaxy is significant and concentrated in the CNR and the inner ring. From the Hα profile we can see a constant, high level in the nucleus, and a decrease along the bar. The profiles display a pronounced peak, coincident with the location of the nuclear ring, at around 10 arcsec radius, and a secondary peak corresponding to the inner ring. Both these peaks appear blue in the $B - I$ colour plot reflecting the underlying SF.

In the close-up of the Hα image of the CNR, the circumnuclear ring is clearly visible, outlined by clumps of SF. For NGC 3351 we have only a ground-based K-band image at our disposal, along with an *HST* H-band image (Paper I). The correspondence of the SF clumps of its nuclear ring as seen in Hα with those seen in the NIR is obvious from

Fig. 2d, where the Hα contours are shown overlaid on the K-band image, and can be further traced in the *HST* image.

A5   NGC 3504

NGC 3504 is an inclined barred galaxy with a nuclear starburst. The double nuclear peak seen in the NIR (Paper I) does not show up in our optical images due to the limited spatial resolution. The $B - I$ colour map shows two curved dust lanes in the bar region, but very little organised dust in the disk region (Fig. 1e). In our Hα image, we see an elliptical region around the nucleus, where SF activity is intense. Outside the CNR, the most luminous HII regions are found near the ends of the bar, but SF is also prominent in the rest of the surrounding disk structure. The radial Hα profile shows a decrease from the nucleus to the radius corresponding to the end of the bar, where enhanced SF activity causes a local maximum in the profile. The $B - I$ radial profile shows a blue peak at the same radius, of about $50''$. The values for the $B - I$ colour are between 1.5 and 2. The central Hα emission in NGC 3504 (Fig. 2e) is elongated in the direction of the double nucleus, as discussed in Paper I.

A6   NGC 3516

This galaxy hosts a Seyfert 1.5 nucleus, but shows little structure in the optical. The images displayed in Fig. 1f have a field of view roughly half as big as the rest of the galaxies, due to the larger distance and smaller angular size of this galaxy. The Hα image shows enhanced emission from the nuclear region, not necessarily from SF but quite possibly from the AGN. We do not detect any sign of SF in the bar or disk of this galaxy. The $B - I$ colour index image shows no convincing structure in the disk, except possibly two redder regions near the ends of the (main) bar. The nucleus is red, as seen in the $B - I$ image and profile, but the white patches seen in the image (Fig. 1f) may be artificial and induced by the nearby presence of the strong nuclear peak. The $B - I$ profile decreases from the nucleus, and becomes stable at 2.5 magnitudes. The Hα emission in the CNR of NGC 3516 (Fig. 2f) is featureless apart from a slight extension in the E-W direction.

A7   NGC 3982

NGC 3982 is one of two barred spirals with a Seyfert 2 nucleus in our sample. The presence of a small bar, at a radius of around 10 arcsec, is evident from the I-band image (Fig. 1g) and from the ellipticity and PA profiles. Further out, the disk is dominated by a spiral pattern. The $B - I$ colour index image displays a rich multi-armed spiral pattern in dust and SF, but is rather smooth near the nucleus. This multi-armed spiral pattern is clear also in the Hα image, with several luminous clumps of SF located mainly in

Figure 2. i. As Fig. 2a now for NGC 4314. **j.** As Fig. 2a, now for NGC 4321.

Figure 2. k. As Fig. 2a now for NGC 5248. **l.** As Fig. 2a, now for NGC 6951.

the arm south of the nucleus, and slightly less in the arm north of it. The nucleus of this galaxy, while neutral in $B-I$, is a relatively strong Hα emitter. We cannot say how much of this emission is due to stars or the AGN, but the latter is a likely contributor. The Hα profile displays a peak in the nucleus, followed by a dip and a secondary peak corresponding in radius to the zone where the SF sites in the spiral arms are located. The profile drops rapidly after a radius of 20-25 arcsec. The $B-I$ profile reflects the Hα peak due to the spiral arm SF as a blue depression. The calibration of our B and I-band data is subject to larger uncertainties than in other galaxies, because no aperture photometry was available for this galaxy. We use average values for the B and I surface brightness and $B-I$ colour, as derived from those other sample galaxies for which calibration was available, and concentrate on the changes in colours rather than on the exact calibrated value.

The CNR of NGC 3982 (Fig. 2g), which may in fact be interpreted as the emission from the relatively compact disk of this galaxy (the scale length of the exponential disk is only 0.6 kpc - Table 1), shows many individual sites of Hα and NIR emission. The relationship between these two kinds of emission is not clear, however, due to the relatively small signal to noise ratio in the areas of interest. Comparison with the *HST* image as shown in Paper I, however, indicates that the same individual regions are responsible for Hα and NIR emission.

A8 NGC 4303

The second Seyfert 2 host galaxy in our sample shows a well-defined bar in the I-band image (Fig. 1h). The $B-I$ image shows two dust lanes in the bar region, which join the inner edge of the spiral arms, and continue as arm dust lanes. The radial profiles in Hα and B show a central peak in surface brightness, followed by a decrease to the radius corresponding to the end of the bar where a secondary peak is located, and a steeper decrease in the disk. The $B-I$ profile reflects these zones as well. The Hα image shows SF activity along the arms and at the ends of the bar, where the bar joins the arms. An especially large concentration of H$_{II}$ regions is located near the northern end of the bar, and a smaller number of H$_{II}$ regions, but of higher luminosity, are found near the southern end. No SF is visible in the bar itself, but the CNR (Fig. 2h) is the site of substantial Hα emission, the morphology of which is however not fully resolved with our imaging. The $B-I$ image reflects in blue colours where these main sites of SF are. The fact that the CNR, so bright in Hα, is not as blue as the regions near the ends of the bar may indicate substantial amounts of dust in the central regions. Alternatively, a substantial fraction of the CNR Hα emission is due to the Seyfert nucleus and not to circumnuclear SF. We refer to Colina et al. (1997) and Colina & Arribas (1999) for more detailed imaging of the CNR of this galaxy.

A9 NGC 4314

NGC 4314 is a symmetrical SBa galaxy with a long stellar bar and two faint outer spiral arms, not visible in our rather shallow I-band image (Fig. 1i). The Hα image shows a number of H$_{II}$ regions forming an incomplete bright nuclear ring, and substantial emission from the (LINER) nucleus. There is no sign of SF activity in the bar or disk of this galaxy. In fact, 94% of the total Hα emission from the galaxy originates in the central region (Pogge 1989). In the $B-I$ colour map, the bar is rather featureless, but in the CNR we see several well-defined blue knots corresponding to the sites of SF, and a pair of short dust lanes which depart from the circumnuclear ring. In the NIR colour index images in Paper I, these dust lanes were seen to form a smooth and continuous ring. The presumed continuation of these dust lanes into the bar cannot be distinguished in the image. The morphology of the galaxy can clearly be recognised in the Hα profile: a nuclear peak followed by a depression, a secondary peak at the radius of the star-forming CNR, and a rapid fall-off outside the CNR. The CNR can be recognised as a dip in the $B-I$ profile, as well as in the B-band profile as a peak due to enhanced blue emission. We find no evidence for a double bar in this galaxy, neither from our own NIR (Paper I) and optical data, nor from the HST NIR image shown in paper I. The ellipticity does go up slightly around 10 arcsec in radius, but this rise is accompanied by large changes in PA; these changes are most probably caused by the strongly emitting distinct regions in the CNR. We thus do not confirm the suggestion by Benedict et al. (1993) and Friedli et al. (1996) of a secondary bar with a semi-major axis length of around 4 arcsec. As in the case of NGC 3982, no aperture photometry in the I-band have been published. We thus took an average calibration number from the rest of our sample and applied this to the I and $B-I$ profiles.

The Hα image of the CNR of NGC 4314 (Fig. 2i) displays four main discrete clumps of massive SF in an incomplete ring. The ring is visible, and appears more complete, in the $J-K$ colour map, which shows no evidence for discrete SF sites. The Hα hot spots are located very near or on the red ring-like region in the colour index map, which points towards an origin of the NIR red colours there in massive SF. The *HST* image (Paper I) shows that at high resolution the NIR "ring" is resolved into many individual hot spots, located along a pair of very tightly wound spiral arms.

A10 NGC 4321

NGC 4321 (M100) is a late-type barred galaxy with well-defined spiral arms and a spectacular central region which only reveals some of its hidden features through the use of the NIR observations. Knapen et al. (1995a,b) discussed in detail the existence and origin of a stellar bar with a large-scale and a small-scale component, a two-armed star-forming spiral in the CNR, and a pair of leading arms inside

the nuclear ring-like region. We have used the same optical images as used by Knapen & Beckman (1996) and refer the reader to that paper for a detailed discussion. In summary, the $B-I$ colour index map shows a pair of curved dust lanes in the bar continuing into the disk spiral arms. A string of HII regions accompanies the dust lanes in the bar. There is abundant Hα emission from the CNR and the disk of this galaxy. Knapen (1998) catalogued almost 2000 individual HII regions from the image shown here and presents a statistical analysis of their properties, but also discusses the Hα morphology. Knapen & Beckman (1996) presented surface brightness profiles for, among other tracers, $B, I, B-I$ and Hα. Although the profiles in the present paper were determined using a different ellipse fitting algorithm, we confirm the main characteristics of the surface brightness and colour profiles. The ellipticity and PA profiles confirm the two parts of the bar (Fig. 1j).

As discussed in detail in the literature (e.g., Knapen et al. 1995a,b, 2000b), images of the CNR of NGC 4321 (Fig. 2j) show good coincidence between the features highlighted by the $J-K$ colour map and the Hα contours. We can see clearly the SF clumps along the arms of the miniature spiral structure (including the characteristic K1 and K2 points – red loci accompanied by massive SF toward the SE and NW of the nucleus).

A11   NGC 5248

Laine et al. (1999) used some of the optical data presented here, in combination with our NIR data from Paper I and adaptive optics NIR imaging, to describe the spiral structure in this galaxy at various scales, including at scales of tens of pc, where it manifests itself in the form of a nuclear grand-design spiral. We refer the reader to Laine et al. for a description of the general disk morphology of NGC 5248, as well as of the CNR. Further detailed studies of the CNR and host galaxy can be found in Laine et al. (2001) and Jogee et al. (2002a,b). Our $B-I$ colour index map (Fig. 1k) shows a pair of curved dust lanes emerging from the nuclear region, more prominent southwest than northeast of the nucleus. Massive SF, as measured by Hα emission, is very strong in the CNR and in the (non-active) nucleus, and is located mainly along the spiral arms in the bar (see Jogee et al. 2002a). The Hα profile outlines the central region with its peak in intensity, followed by a second maximum that corresponds to the region of the arms where the SF is found. In the region of the second maximum a small bump in the $B-I$ colour profile is also visible. The ellipticity and PA profiles are remarkably flat.

NGC 5248 (Fig. 2k) also exhibits massive SF sites mainly situated in the nuclear ring, seen in Hα and in the *HST H*-band image (Paper I). The massive SF activity seems not to extend to the spiral arms and is confined to the nuclear ring and the region immediately surrounding it.

A12   NGC 6951

Our images of this galaxy (Fig. 1l) suffer from rather poor spatial resolution, but the strong bar and main spiral arms in the disk can easily be identified. The $B-I$ image shows a pair of curved dust lanes which emerges from the CNR and runs roughly parallel to the spiral arms. The enhanced SF activity in the CNR is obvious from the blue colour in the $B-I$ map and from the Hα image, but the resolution in the images is too poor to show much detail (compare, e.g., to the H-band HST image shown in Paper I). The Hα image shows SF activity across the disk, but none is observed along the bar. There is also some Hα emission from the (LINER/Seyfert) nucleus.

We encountered two problems in the process of the ellipse fitting, resulting in higher than normal uncertainties: the original images had saturated centres, and no aperture photometry for the I-band was found. We thus used average values for μ_I and $B-I$ as labelled in the appropriate profiles in Fig. 1l. We see no evidence for an inner bar from our combined optical and NIR profile fits, contrary to the suggestion of Wozniak et al. (1995) as based on optical imaging, a suggestion which, however, could not be unambiguously confirmed by the same team from their NIR imaging (Friedli et al. 1996).

NGC 6951 (Fig. 2l), like NGC 5248, shows miniature spiral structure in the *HST* image, but this spiral is not resolved in our Hα image and the clumps of massive SF seem to be confined to the ring. As in, e.g., NGC 4314, the regions of massive SF as traced by Hα emission coincide in radius with the red "ring" as traced by the $J-K$ image.

This paper has been produced using the Royal Astronomical Society/Blackwell Science L^ATEX style file.

This figure "knapen.fig1a.jpg" is available in "jpg" format from:

http://arxiv.org/ps/astro-ph/0207258v1

This figure "knapen.fig1b.jpg" is available in "jpg" format from:

http://arxiv.org/ps/astro-ph/0207258v1

This figure "knapen.fig1c.jpg" is available in "jpg" format from:

http://arxiv.org/ps/astro-ph/0207258v1

This figure "knapen.fig1d.jpg" is available in "jpg" format from:

http://arxiv.org/ps/astro-ph/0207258v1

This figure "knapen.fig1e.jpg" is available in "jpg" format from:

http://arxiv.org/ps/astro-ph/0207258v1

This figure "knapen.fig1f.jpg" is available in "jpg" format from:

http://arxiv.org/ps/astro-ph/0207258v1

This figure "knapen.fig1g.jpg" is available in "jpg" format from:

http://arxiv.org/ps/astro-ph/0207258v1

This figure "knapen.fig1h.jpg" is available in "jpg" format from:

http://arxiv.org/ps/astro-ph/0207258v1

This figure "knapen.fig1i.jpg" is available in "jpg" format from:

http://arxiv.org/ps/astro-ph/0207258v1

This figure "knapen.fig1j.jpg" is available in "jpg" format from:

http://arxiv.org/ps/astro-ph/0207258v1

This figure "knapen.fig1k.jpg" is available in "jpg" format from:

http://arxiv.org/ps/astro-ph/0207258v1

This figure "knapen.fig1l.jpg" is available in "jpg" format from:

http://arxiv.org/ps/astro-ph/0207258v1

This figure "knapen.fig2a-d.jpg" is available in "jpg" format from:

http://arxiv.org/ps/astro-ph/0207258v1

This figure "knapen.fig2e-h.jpg" is available in "jpg" format from:

http://arxiv.org/ps/astro-ph/0207258v1

This figure "knapen.fig2i-l.jpg" is available in "jpg" format from:

http://arxiv.org/ps/astro-ph/0207258v1